

Carbon and sulfur budget of the silicate Earth explained by accretion of differentiated planetary embryos

Yuan Li^{1*}†, Rajdeep Dasgupta^{1*}, Kyusei Tsuno¹, Brian Monteleone² and Nobumichi Shimizu²

The abundances of volatile elements in the Earth's mantle have been attributed to the delivery of volatile-rich material after the main phase of accretion^{1–3}. However, no known meteorites could deliver the volatile elements, such as carbon, nitrogen, hydrogen and sulfur, at the relative abundances observed for the silicate Earth⁴. Alternatively, Earth could have acquired its volatile inventory during accretion and differentiation, but the fate of volatile elements during core formation is known only for a limited set of conditions^{4–8}. Here we present constraints from laboratory experiments on the partitioning of carbon and sulfur between metallic cores and silicate mantles under conditions relevant for rocky planetary bodies. We find that carbon remains more siderophile than sulfur over a range of oxygen fugacities; however, our experiments suggest that in reduced or sulfur-rich bodies, carbon is expelled from the segregating core. Combined with previous constraints⁹, we propose that the ratio of carbon to sulfur in the silicate Earth could have been established by differentiation of a planetary embryo that was then accreted to the proto-Earth. We suggest that the accretion of a Mercury-like (reduced) or a sulfur-rich (oxidized) differentiated body—in which carbon has been preferentially partitioned into the mantle—may explain the Earth's carbon and sulfur budgets.

The origin and distribution of Earth's volatiles, such as carbon and sulfur, are critical for understanding Earth's evolution and formation of the biosphere. However, the processes of volatiles acquisition into the early Earth remain poorly understood. One widely accepted model suggests that the Earth formed from chondritic material completely devoid of volatiles, and the Earth's volatiles were delivered by volatile-rich chondritic material in the form of late veneer after complete core–mantle segregation^{1–3}. The strongest argument supporting this model arises from the observation that the ratios of sulfur, selenium and tellurium in the mantle are chondritic^{1,3}. A competing model assumes that Earth acquired its volatiles from volatile-depleted material as accretion progressed^{8–11}. In this model volatiles were thus present during the stages of Earth's differentiation and core formation. For example, it has been shown that the mantle sulfur budget can be established from accretion of chondritic material⁹, without need of the addition of a late veneer. This notion is supported by the non-chondritic sulfur isotopic composition of Earth's mantle, which can be explained if sulfur isotopes are fractionated between the Earth's core and mantle¹². The copper¹³, silver¹⁴ and carbon^{11,15} isotopic compositions of Earth's mantle also strongly support this model and compromise significantly the late veneer model.

The carbon and sulfur abundances in Earth's present mantle are 35–115 ppm (parts per mil by weight)¹⁶ and 150–250 ppm (refs 1,17), respectively, and the C/S ratio (0.14–0.76) of Earth's present mantle is comparable to those observed for carbonaceous chondrites (0.2–0.7; Supplementary Fig. 1). Therefore, any models that try to constrain the accretion process of Earth's carbon and sulfur may have to be consistent with these constraints. However, the fate of carbon and sulfur in planetary magma oceans (MOs) remains poorly understood^{3–7}. In this study, we investigate systematically the effects of pressure, temperature, melt composition, melt water content, and fO_2 on the partitioning of carbon and sulfur between Fe-rich alloy melt and silicate melt. Using the newly obtained partitioning data and previous constraints⁹, we show that the carbon abundance and C/S ratio of Earth's present mantle can be established by adding a Mercury-like or a S-rich differentiated body into the growing Earth during accretion and core formation.

Experiments in graphite capsule have been performed at 1.5–8.0 GPa, 1,600–2,200 °C, and oxygen fugacities of IW-0.4 to IW-5.3 (IW refers to fO_2 , defined by the coexistence of Fe and FeO) to determine simultaneously the partition coefficients of carbon and sulfur between Fe–Ni ± S ± Si alloy and silicate melt (Supplementary Fig. 2), using a piston cylinder or multi-anvil apparatus (see Methods). The results show that C-solubility in Si-free or low-S alloy melt is ~5.5 wt% (Supplementary Fig. 3), while C-solubility decreases to less than 1 wt% with increasing Si or S content in the alloy (Fig. 1a,b). C-solubility in silicate melt, analysed by secondary ionization mass spectrometry (SIMS; see Methods), is mainly controlled by fO_2 and melt H₂O content (Supplementary Fig. 4). At fO_2 from IW-0.6 to IW-1.5, C-solubility drops from ~90 to ~10 ppm. However, at fO_2 < IW-1.5, C-solubility increases up to 240 ppm with decreasing fO_2 if the melt H₂O content is 0.3–0.8 wt%; whereas C-solubility only decreases or slightly increases at fO_2 below IW-3 if melt H₂O < 0.2 wt%. Raman and Fourier-transformed infrared (FTIR) spectra show that the silicate glass with fO_2 around IW-0.6 contained ~10–30 ppm carbon as CO₃^{2–}; however, at fO_2 < IW-1, the CO₃^{2–} peak was undetectable in FTIR spectra, but H₂ and CH₄ peaks are present in the Raman spectra (Supplementary Fig. 5). The strong correlations between the Raman peak intensities of H₂ and CH₄ and between the non-hydroxyl hydrogen and non-carbonate carbon (Supplementary Fig. 6) suggests that CO₃^{2–} and CH₄ are the main carbon species in this study. $D_C^{\text{alloy/silicate}}$ (concentration of carbon by weight in the alloy melt divided by concentration of carbon by weight in the silicate melt) varied from 130 to 4,600, and the range is mainly governed by fO_2 and melt hydration (Fig. 1c). At fO_2 > IW-1.5,

¹Department of Earth Science, Rice University, 6100 Main Street, MS 126, Houston, Texas 77005, USA. ²Department of Geology and Geophysics, Woods Hole Oceanographic Institution, Woods Hole, Massachusetts 02543, USA. †Present address: Guangzhou Institute of Geochemistry, Chinese Academy of Sciences, Guangzhou 510640, China. *e-mail: Yuan.Li@gig.ac.cn; Rajdeep.Dasgupta@rice.edu

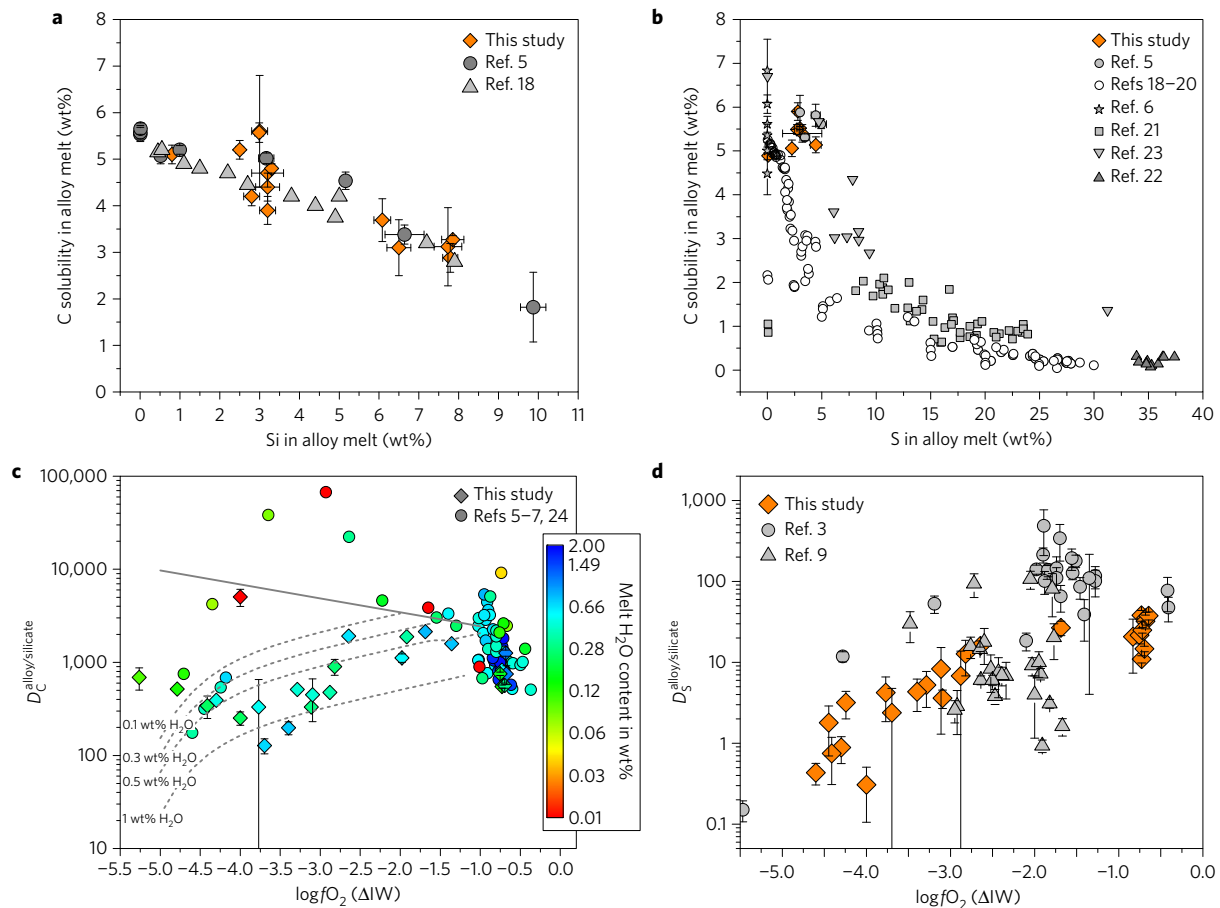


Figure 1 | Experimentally measured carbon solubility in alloy melt and measured partition coefficients of carbon and sulfur between alloy melt and silicate melt. a, Carbon solubility decreases with increasing Si content in alloy. **b**, Carbon solubility decreases with increasing S content in alloy. **c**, fO_2 and silicate melt hydration play a major role in controlling $D_C^{\text{alloy/silicate}}$. The solid and dashed curves are calculated $D_C^{\text{alloy/silicate}}$ values for a mid-ocean ridge basalts (MORB)-like melt at 6 GPa and 2,000 °C, using equations (3) and (4) in the Methods, respectively. **d**, $D_S^{\text{alloy/silicate}}$ in general decreases with decreasing fO_2 .

the increase in $D_C^{\text{alloy/silicate}}$ with decreasing fO_2 is mainly due to the decreased CO_3^{2-} in silicate melt; while the decrease in $D_C^{\text{alloy/silicate}}$ at $fO_2 < IW-1.5$ or $IW-3$ is mainly due to the increased CH_4 content in silicate melt. $D_S^{\text{alloy/silicate}}$ (concentration of sulfur by weight in the alloy melt divided by concentration of sulfur by weight in the silicate melt) varied from 0.4 to 38 (Fig. 1d), generally decreasing with decreasing fO_2 . $D_S^{\text{alloy/silicate}}$ is always significantly lower than $D_C^{\text{alloy/silicate}}$, with the $D_C^{\text{alloy/silicate}}/D_S^{\text{alloy/silicate}}$ ratio increasing from about 20 to 1,000 as fO_2 decreases from $IW-0.6$ to $IW-4.7$ (Supplementary Fig. 7).

Our $D_C^{\text{alloy/silicate}}$ and $D_S^{\text{alloy/silicate}}$ data indicate that if carbon and sulfur were simultaneously delivered to Earth's early MO with a chondritic ratio, segregation of Fe-rich alloy phase from the MO must cause greater depletion of carbon relative to sulfur in the silicate mantle, and the nearly chondritic C/S ratio observed for Earth's present mantle cannot be obtained (Supplementary Figs 9 and 10). The sulfur abundance in Earth's present mantle can, however, be formed during Earth's accretion⁹. We below evaluate two processes that may have occurred during Earth's accretion and core formation but can effectively enhance Earth's mantle carbon abundance and thus explain the C/S ratio observed for Earth's present mantle.

The low carbon solubility in Si-rich alloy may result in the saturation of graphite or diamond in the alloy in a highly reduced MO where up to 10 wt% Si could be in the alloy (Fig. 1a). Figure 2 shows that for a highly reduced planetary MO with the alloy/silicate mass ratio of equilibration lower than that of Mars, the saturation of graphite or diamond can be obtained with 2,000 ppm initial carbon in the MO. A lower alloy/silicate mass ratio is needed when the initial carbon content in the MO is <2,000 ppm. For

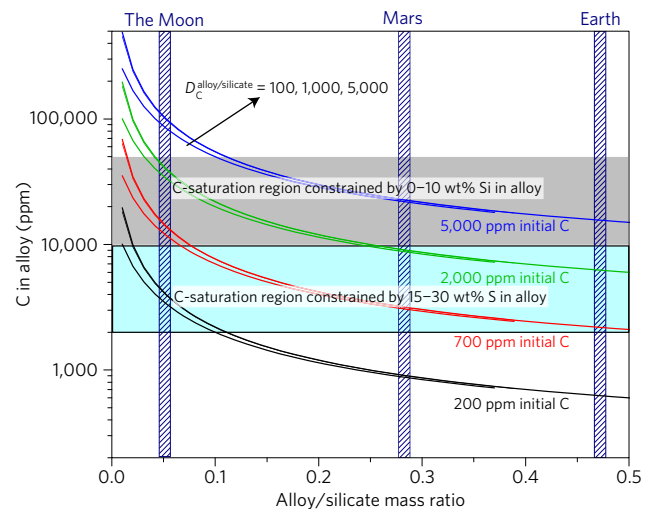


Figure 2 | Calculated carbon content in alloy as a function of alloy/silicate mass ratio and initial carbon content in the MO. The carbon-saturation regions are constrained by carbon solubility in the alloy containing S or Si. Alloy: silicate mass ratio at which calculated carbon content of alloy melt exceeds the alloy saturation values, carbon exsolves from the segregating core. Note that using different $D_C^{\text{alloy/silicate}}$ values from 100 to 5,000 negligibly affect carbon content in the alloy. This figure illustrates that alloy in an MO of a highly reduced or a sulfur-rich and oxidized body can obtain graphite or diamond saturation.

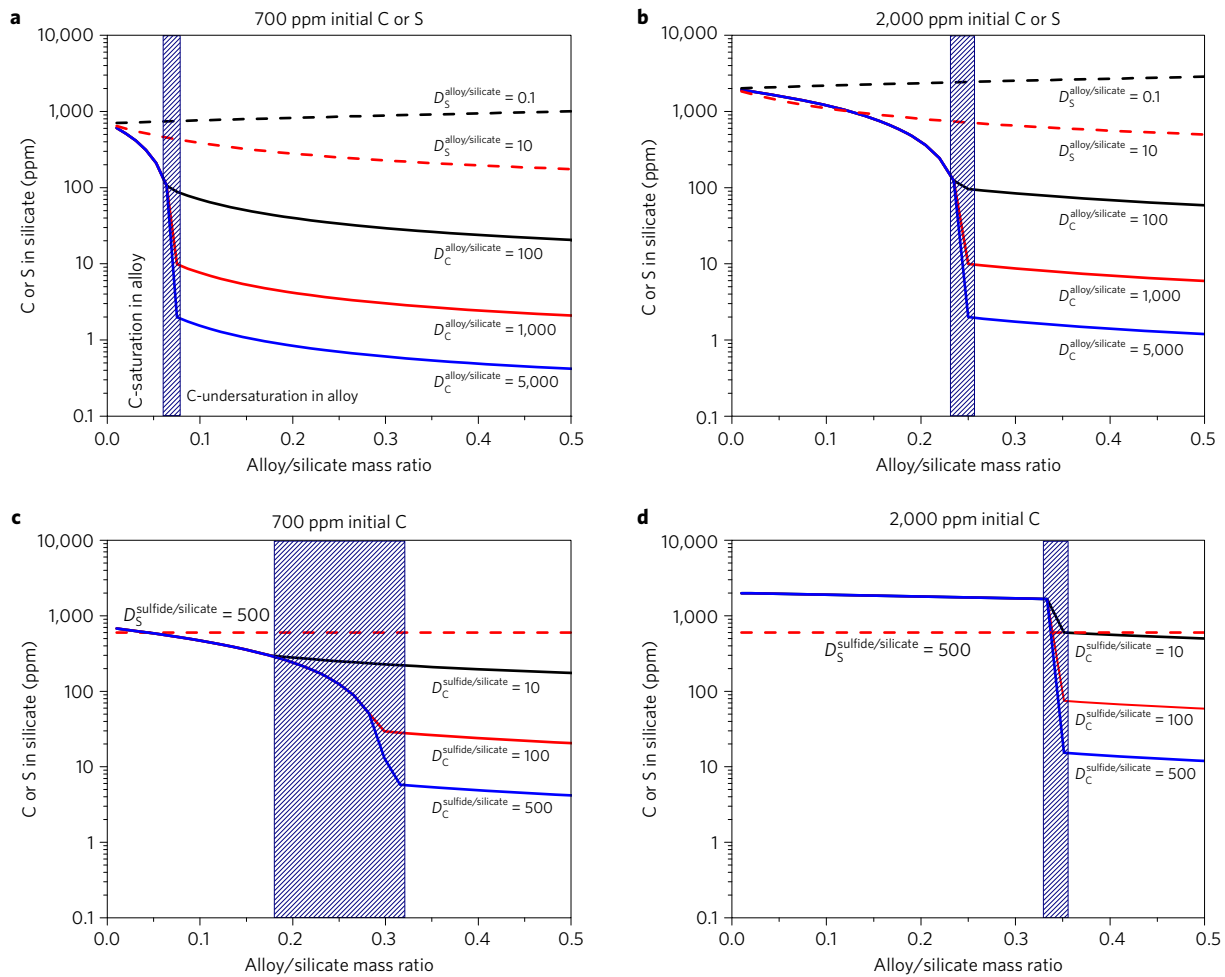


Figure 3 | Calculated carbon and sulfur contents in the silicate of a highly reduced or an S-rich body. a, b, The carbon solubility in the alloy at reducing conditions is fixed at 1 wt% and the $D_C^{\text{alloy/silicate}}$ and $D_S^{\text{alloy/silicate}}$ used are from highly reduced conditions in Fig. 1. **c, d**, Carbon solubility in the S-rich alloy (30 wt% S) is fixed at 0.3 wt%. $D_S^{\text{sulfide/silicate}}$ of 500, the maximum value from experiments on sulfide solubility in silicate melt (ref. 9), was used to constrain the mantle sulfur. For $D_C^{\text{sulfide/silicate}}$ calculations, see Supplementary Information. The vertical bands separate the conditions of graphite/diamond saturation to undersaturation in alloy.

example, when the initial carbon content is 700 ppm, as has been estimated for the bulk Earth²⁵, the alloy/silicate mass ratio needs to be <0.05, which is similar to the alloy/silicate mass ratio of the Moon. On the other hand, in a S-rich MO, where the alloy can contain up to 30 wt% sulfur but less than 0.3 wt% carbon (Fig. 1b), the saturation of graphite or diamond in the S-rich alloy (sulfide) can be obtained even with 200 ppm initial carbon in the MO (Fig. 2).

In an MO where the alloy is saturated with graphite or diamond, the total carbon content in the silicate would be higher than the carbon content constrained by the equilibrium alloy–silicate partitioning. Figure 3 shows the calculated carbon and sulfur contents in the silicate, as a function of alloy/silicate mass ratio, initial carbon or sulfur content in the MO, and $D_S^{\text{alloy/silicate}}$ and $D_C^{\text{alloy/silicate}}$, or $D_S^{\text{sulfide/silicate}}$ and $D_C^{\text{sulfide/silicate}}$. In Fig. 3a,b, the carbon solubility in alloy is fixed to be 1 wt%, which corresponds to a highly reduced MO; whereas in Fig. 3c,d the carbon solubility in alloy is fixed to be 0.3 wt%, which corresponds to an S-rich and oxidized MO. Figure 3a,b shows that, for a highly reduced rocky body with alloy/silicate mass ratio between 0.06 and 0.24, the carbon content in the silicate could be between 100 and 2,000 ppm if the initial carbon content in the magma ocean is between 700 and 2,000 ppm. The high end of these initial carbon contents are comparable to those of reduced E-type chondrites (Supplementary Fig. 1). Figure 3c,d

shows that, for an S-rich and oxidized MO, the resulting carbon content in the silicate could be even higher. It is worth noting that the silicate is always more enriched in sulfur relative to carbon at reduced conditions, because highly reduced conditions correspond to low $D_S^{\text{alloy/silicate}}$ values (Fig. 1d). Therefore, the silicate of a highly reduced body is potentially rich in both sulfur and carbon. Such a reduced body may be similar to Mercury^{26,27} but have a smaller core/mantle mass ratio than that of the present-day Mercury. The observed high sulfur content in mercurian surface has been ascribed to the highly reduced conditions in mercurian MO^{26,27}, and is also consistent with our measured low $D_S^{\text{alloy/silicate}}$ values at highly reduced conditions. High carbon content was also observed in mercurian surface²⁸, which was thought to be delivered by micrometeorites²⁹. However, as discussed above, saturation and subsequent flotation of graphite in a highly reduced MO may potentially lead to a high carbon content of Mercury’s surface.

Accordingly, adding such a highly reduced, Mercury-like body or an S-rich, oxidized body to the growing Earth should remarkably enhance the carbon abundance in Earth’s mantle. Mass balance calculations show that adding such a body of 5–30% of Earth’s present mass would enhance the carbon abundance in Earth’s present mantle to a few tens to hundreds ppm (Fig. 4). The merger of the core of the reduced or S-rich, oxidized body with Earth’s core may negligibly affect the carbon content in the silicate

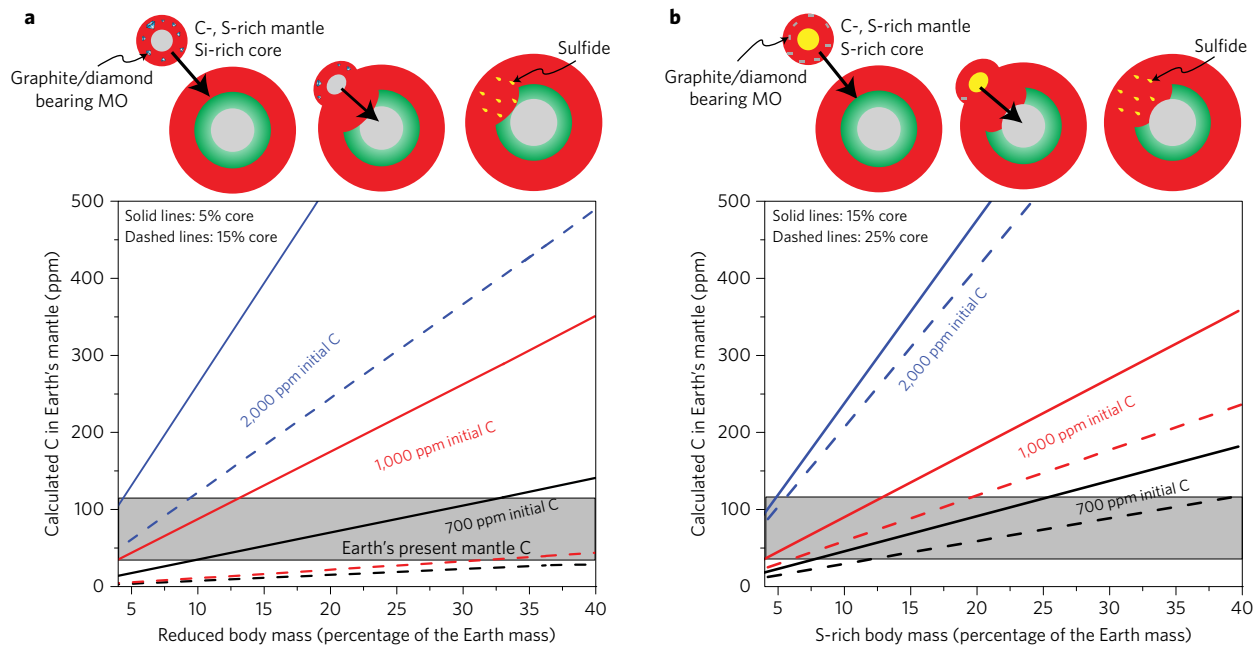


Figure 4 | Carbon content of the Earth's mantle after accretion of a highly reduced or a sulfur-rich planetary embryo. a, b, Mantle of accreting bodies would be carbon-rich, as indicated by 'graphite' or 'diamond' in the cartoon, through carbon saturation in alloy. The core of the impacting body merges with proto-Earth's core, and excess sulfur is removed to the core as sulfide. The addition of a reduced (**a**) or S-rich (**b**) body of 5–30% of the Earth's mass does not violate the constraints of the Si (ref. 8) and/or S (ref. 9) in the Earth's core, if the proto-Earth's core is S- or Si-poor.

mantle. Adding such an impactor body with more than 2,000 ppm carbon, although highly unlikely considering the high volatility of carbon and the low carbon contents in the reduced chondrites (Supplementary Fig. 1), may cause excess carbon relative to the present-day mantle value, but a higher core/mantle ratio than presented in Fig. 4 would effectively decrease the carbon content in the mantle of the impactor. Therefore, the carbon abundance of Earth's present mantle can be established well if a highly reduced or an S-rich and oxidized body was added to the growing Earth. However, since a few hundreds to thousands ppm sulfur may be in the mantle of the highly reduced or S-rich and oxidized body (Fig. 3), and since sulfur abundance in Earth's mantle can be established alone by Earth's core–mantle segregation⁹, additional processes are needed to remove the excess sulfur after addition of the highly reduced or S-rich body to the growing Earth. The f_{O_2} of the growing Earth at the late stage, in particular, may be several log units higher than that of the reduced body. Consequently, sulfur from the mantle of either the reduced body or the S-rich body may form sulfide in the post-MO mantle, the segregation of which into Earth's core should remove the excess sulfur without affecting the carbon content in Earth's mantle because of the low carbon solubility in sulfide (Fig. 1b). Although it is unclear at this stage whether the proposed scenario can account for the ratios of other chalcophile elements, the addition of a highly reduced rocky body to the growing Earth can also potentially explain the superchondritic Sm/Nd and $^{142}\text{Nd}/^{144}\text{Nd}$ anomaly observed for Earth's present mantle³⁰. The segregation of sulfide from Earth's mantle into the core during late differentiation is also consistent with the observed Cu isotopic composition of Earth's mantle¹³.

Methods

Methods, including statements of data availability and any associated accession codes and references, are available in the [online version of this paper](#).

Received 11 March 2016; accepted 27 July 2016;
published online 5 September 2016

References

- Wang, Z. & Becker, H. Ratios of S, Se and Te in the silicate Earth require a volatile-rich late veneer. *Nature* **499**, 328–331 (2013).
- Albarede, F. Volatile accretion history of the terrestrial planets and dynamic implications. *Nature* **461**, 1227–1233 (2009).
- Rose-Weston, L., Brenan, J. M., Fei, Y., Secco, R. A. & Frost, D. J. Effect of pressure, temperature, and oxygen fugacity on the metal–silicate partitioning of Te, Se and S: implications for Earth differentiation. *Geochim. Cosmochim. Acta* **73**, 4598–4615 (2009).
- Bergin, E. A., Blake, G. A., Ciesla, F., Hirschmann, M. M. & Li, J. Tracing the ingredients for a habitable Earth from interstellar space through planet formation. *Proc. Natl Acad. Sci. USA* **112**, 8965–8970 (2015).
- Li, Y., Dasgupta, R. & Tsuno, K. The effects of sulfur, silicon, water, and oxygen fugacity on carbon solubility and partitioning in Fe-rich alloy and silicate melt systems at 3 GPa and 1600 °C: implications for core–mantle differentiation and degassing of magma oceans and reduced planetary mantles. *Earth Planet. Sci. Lett.* **415**, 54–66 (2015).
- Dasgupta, R., Chi, H., Shimizu, N., Buono, A. S. & Walker, D. Carbon solution and partitioning between metallic and silicate melts in a shallow magma ocean: implications for the origin and distribution of terrestrial carbon. *Geochim. Cosmochim. Acta* **102**, 191–212 (2013).
- Chi, H., Dasgupta, R., Duncan, M. S. & Shimizu, N. Partitioning of carbon between Fe-rich alloy melt and silicate melt in a magma ocean—Implications for the abundance and origin of volatiles in Earth, Mars, and the Moon. *Geochim. Cosmochim. Acta* **139**, 447–471 (2014).
- Rubie, D. C. *et al.* Accretion and differentiation of the terrestrial planets with implications for the compositions of early-formed solar system bodies and accretion of water. *Icarus* **248**, 89–108 (2015).
- Boujibar, A. *et al.* Metal–silicate partitioning of sulphur, new experimental and thermodynamic constraints on planetary accretion. *Earth Planet. Sci. Lett.* **391**, 42–54 (2014).
- Wood, B. J., Halliday, A. N. & Rehkamper, M. Volatile accretion history of the Earth. *Nature* **467**, E6–E7 (2010).
- Wood, B. J., Li, J. & Shahar, A. Carbon in the core: its influence on the properties of core and mantle. *Rev. Mineral. Geochem.* **75**, 231–250 (2013).
- Labidi, J., Cartigny, P. & Moreira, M. Non-chondritic sulphur isotope composition of the terrestrial mantle. *Nature* **501**, 208–211 (2013).
- Savage, P. S. *et al.* Copper isotope evidence for large-scale sulphide fractionation during Earth's differentiation. *Geochem. Perspect. Lett.* **1**, 53–64 (2015).
- Schönbächler, M., Carlson, R. W., Horan, M. F., Mock, T. D. & Hauri, E. H. Heterogeneous accretion and the moderately volatile element budget of Earth. *Science* **328**, 884–887 (2010).

15. Horita, J. & Polyakov, V. B. Carbon-bearing iron phases and the carbon isotope composition of the deep Earth. *Proc. Natl Acad. Sci. USA* **112**, 31–36 (2015).
16. Rosenthal, A., Hauri, E. & Hirschmann, M. Experimental determination of C, F, and H partitioning between mantle minerals and carbonated basalt, CO₂/Ba and CO₂/Nb systematics of partial melting, and the CO₂ contents of basaltic source regions. *Earth Planet. Sci. Lett.* **412**, 77–87 (2015).
17. McDonough, W. F. & Sun, S.-S. The composition of the Earth. *Chem. Geol.* **120**, 223–253 (1995).
18. Bouchard, D. B. & Bale, C. W. Simultaneous optimization of thermochemical data for liquid iron alloys containing C, N, Ti, Si, Mn, S, and P. *Metall. Mater. Trans. B* **26**, 467–484 (1995).
19. Tsybulov, L. B. & Tsemekhman, L. S. Solubility of carbon in sulfide melts of the system Fe-Ni-S. *Russ. J. Appl. Chem.* **74**, 925–929 (2001).
20. Wang, C., Hiram, J., Nagasaka, T. & Ban-Ya, S. Phase equilibrium of liquid Fe-S-C ternary system. *ISIJ Int.* **31**, 1292–1299 (1991).
21. Tsuno, K. & Dasgupta, R. Fe-Ni-Cu-C-S phase relations at high pressures and temperatures—The role of sulfur in carbon storage and diamond stability at mid- to deep-upper mantle. *Earth Planet. Sci. Lett.* **412**, 132–142 (2015).
22. Deng, L., Fei, Y., Liu, X., Gong, Z. & Shahar, A. Effect of carbon, sulfur and silicon on iron melting at high pressure: implications for composition and evolution of the planetary terrestrial cores. *Geochim. Cosmochim. Acta* **114**, 220–233 (2013).
23. Zhang, Z., Lentsch, N. & Hirschmann, M. M. Carbon-saturated monosulfide melting in the shallow mantle: solubility and effect on solidus. *Contrib. Mineral. Petrol.* **170**, 1–13 (2015).
24. Armstrong, L. S., Hirschmann, M. M., Stanley, B. D., Falksen, E. G. & Jacobsen, S. D. Speciation and solubility of reduced C–O–H–N volatiles in mafic melt: implications for volcanism, atmospheric evolution, and deep volatile cycles in the terrestrial planets. *Geochim. Cosmochim. Acta* **171**, 283–302 (2015).
25. Marty, B. The origins and concentrations of water, carbon, nitrogen and noble gases on Earth. *Earth Planet. Sci. Lett.* **313**, 56–66 (2012).
26. Malavergne, V., Toplis, M. J., Berthet, S. & Jones, J. Highly reducing conditions during core formation on Mercury: implications for internal structure and the origin of a magnetic field. *Icarus* **206**, 199–209 (2010).
27. McCubbin, F. M., Riner, M. A., Vander Kaaden, K. E. & Burkemper, L. K. Is Mercury a volatile-rich planet? *Geophys. Res. Lett.* **39**, L09202 (2012).
28. Peplowski, P. N. *et al.* Constraints on the abundance of carbon in near-surface materials on Mercury: results from the MESSENGER Gamma-Ray Spectrometer. *Planet. Space. Sci.* **108**, 98–107 (2015).
29. Syal, M. B., Schultz, P. H. & Riner, M. A. Darkening of Mercury's surface by cometary carbon. *Nat. Geosci.* **8**, 352–356 (2015).
30. Wohlers, A. & Wood, B. J. A Mercury-like component of early Earth yields uranium in the core and high mantle ¹⁴²Nd. *Nature* **520**, 337–340 (2015).

Acknowledgements

Y.L. thanks A. Boujibar for discussion on topics related to the present work. NASA grant NNX13AM51G to R.D. supported this work. R.D. also acknowledges a NSF grant EAR-1053816 that established the Rice University's multi-anvil facility used in this study.

Author contributions

Y.L. and R.D. conceived the project. Y.L. performed all the experiments, FTIR and Raman analyses of experimental glasses. B.M., Y.L. and N.S. performed the SIMS analyses. K.T. performed the electron microprobe analyses. Y.L. and R.D. analysed and interpreted all the data and co-wrote the paper. All authors commented on the manuscript.

Additional information

Supplementary information is available in the [online version of the paper](#). Reprints and permissions information is available online at www.nature.com/reprints. Correspondence and requests for materials should be addressed to Y.L. or R.D.

Competing financial interests

The authors declare no competing financial interests.

Methods

Starting materials. Starting materials included ~60–70 wt% silicate powder of natural Knippa basanite and synthetic basaltic glass with a composition similar to that of mid-ocean ridge basalts (MORB) as used in previous studies^{5–7}, and 30–40 wt% metal powder of Fe–Ni–S, Fe–Ni–Si, or Fe–Ni–S–Si mixture (Supplementary Table 1). The natural Knippa basanite and synthetic basaltic glass were dehydrated at 1,000 °C and $\log f_{\text{O}_2}$ of ~FMQ-2 (FMQ refers to the oxygen fugacity value equivalent to that defined by the coexistence of fayalite, magnetite and quartz) using a CO–CO₂ Deltech gas mixing furnace for 24 h in order to obtain a relatively low water content and to reduce the Fe³⁺ in the silicate. Homogeneous metal mixtures were prepared from analytical grade Fe, Ni, Si and FeS powders, and were stored in a desiccator at 100 °C for ≥24 h before loading into graphite capsules and subjecting them to high *P–T* experimental conditions.

High-pressure experiments. All the experiments were conducted at Rice University. Experiments at 1.5–3 GPa were conducted using an end-loaded piston cylinder device. All experiments at 4–8 GPa were conducted using a Walker-type multi-anvil device. Piston cylinder experiments employed a 1/2-inch assembly with BaCO₃ pressure-transmitting medium, MgO spacers, and straight-walled graphite furnace. For multi-anvil experiments, WC anvils with 12 mm truncations, cast MgO–Al₂O₃–SiO₂ octahedral with 18 mm edge lengths and integrated gasket fins, and straight-walled graphite heaters with molybdenum end rings were used. The detailed descriptions of pressure calibration and the assemblies used for piston cylinder and multi-anvil experiments can be found in previous studies^{5–7,21,31,32}. Graphite capsules were used in order to study carbon solubility in silicate melt and Fe-rich alloy melt. All the experiments were pressurized first at room temperature and then heated at a rate of 100 °C min⁻¹. In order to reduce porosity in the graphite capsules and prevent leakage of alloy melt, all the experiments were held at 850 °C for 1–3 h, and then raised to the desired, nominal temperature of the experiment. During the run, temperature was monitored and controlled with a type-C thermocouple next to the capsule and oriented axially with respect to the heater. *P–T* uncertainties are estimated to be ±0.1 GPa, ±15 °C for piston cylinder experiments and ±0.3 GPa, ±10 °C for multi-anvil experiments. All experiments were brought down to room temperatures within 10–20 s by switching off the electric power to the graphite heater.

Texture of quench products. All the experiments produced quenched blobs of alloy melt embedded in silicate melts (Supplementary Fig. 2 and Supplementary Table 1). The alloy melt was exsolved into a few phases during quench (Supplementary Fig. 2). Silicate melt in some runs was not quenched into glass and fine mineral crystals were produced during quench. Only the samples containing silicate glass were measured below to determine the carbon solubility and partitioning between the Fe-rich alloy melt and silicate melt, whereas all the samples, including the samples with unquenchable silicate melt, were analysed to determine the partition coefficient of sulfur between the Fe-rich alloy melt and silicate melt.

Analyses of experimental products and key results. Quantitative, WDS analyses of major and minor element compositions of silicate melt and alloy melt were carried out on a Cameca SX-100 electron microprobe in NASA-Johnson Space Center (NASA-JSC). For the measurement of major elements in silicate glasses, a beam diameter of 20 μm, 15 kV accelerating voltage, and 10 nA beam current for all elements (except for S which was analysed at 15 kV and 80 nA) were used both for standardization and sample measurement. Both synthetic and natural standards were used for calibration: oligoclase for Na, orthoclase for K, fayalite for Fe, rutile for Ti, troilite for S, chromite for Cr, metallic Ni for Ni, apatite for P, rhodonite for Mn, and basaltic glass for Al, Ca, Si and Mg. The peak counting time was 20 s—except for S, Na and K, which was measured for 40, 10 and 10 s, respectively. For analysing the quenched alloy melt, the samples and standards were uncoated but surrounded with silver-bearing conductive varnish to avoid charging during EPMA analysis. The standards used included pure Ni metal for Ni, pure Fe metal for Fe, pure Si metal for Si, natural troilite, FeS for sulfur, and synthetic Fe₃C for carbon. Analytical conditions for alloy melt analysis were 12 kV accelerating voltage, 80 nA beam current, and 20–30 micron beam diameter. Carbon was analysed using a LPC2 multilayer spectrometer, and counting times were 10 s at peak and 5 s at each background. An anti-contaminant device cooled with liquid N₂ was used to minimize carbon blank concentration, and the amount of carbon contamination from the sample surface was estimated to be ~0.4 wt% by analysing pure Si and Fe metals, according to the protocol of Dasgupta and Walker³³.

The major and minor element compositions measured for silicate melts and alloy melts are tabulated in Supplementary Table 2. Compared to the composition of starting silicate, the silicate melt compositions from the runs at oxidized conditions (for example, runs MA94, MA95 and G325) were moderately FeO-rich (up to 17 wt%), due to oxidation of a small fraction of Fe in the alloy. However, the silicate melts in the runs at reduced conditions (for example, runs MA66, MA68 and G327) became SiO₂-rich (up to 55 wt%) but depleted in FeO (down to 0.4 wt%) due to the reduction of FeO in the silicate melt by Si in the alloy melt via the

reaction of 2FeO (silicate) + Si (alloy) = SiO₂ (silicate) + 2Fe (alloy). The values of silicate melt NBO/T (non-bridging oxygens per tetrahedral cations) are in the range from 0.68 to 1.37 (see Supplementary Table 2). The Ni content of alloy melt was very close to 5 wt%, and the Fe content of alloy melt ranged from ~82 to 90 wt%. The sulfur content in alloy melt ranged from ~0 to 5.6 wt%, while Si content in alloy melt ranged from <0.1 to ~7.8 wt%. The carbon content in alloy melt ranged from 3.0 to 5.9 wt%, and is not dependent on pressure or temperature (Supplementary Fig. 3), but depends significantly on the S and Si contents in the alloy melt (Fig. 1).

The bulk carbon and water contents in the quenched silicate glasses were determined using a Cameca IMS 1280 ion microprobe at Woods Hole Oceanographic Institution, using the same procedures and standardization as described in previous studies^{5–7}. The Cs⁺ primary beam current was 1 nA, and the beam was rastered over ~30 × 30 square micron area. A secondary voltage was 10 kV, with electron gun compensation for positive charge buildup on the sample surface. A secondary field aperture was used to block transmission of ions from outside of the innermost ~10 × 10 square microns of the analysis crater, therefore effectively minimizing any potential carbon surface contamination in the measurement. Calibration for H₂O and CO₂ were obtained by replicate measurements of ¹²C/³⁰Si and ¹H¹⁶O/³⁰Si ratios in standard glasses of basaltic composition. CO₂ and H₂O contents in the standards determined by Fourier transform infrared (FTIR) spectroscopy and/or manometry can be found in Helo and colleagues³⁴. About 3–6 spots were analysed for each sample glass, and each spot included 10 analytical cycles. During each cycle, a sequence of ¹²C, ¹H¹⁶O and ³⁰Si was recorded and the intensity ratios of ¹²C/³⁰Si and ¹H¹⁶O/³⁰Si were converted to C and H (reported as H₂O) contents. After each three analytical spots on the sample glass, one or two analyses were performed on the standard glass (ALV 519-4-1) to check the possible deviation and accuracy during the analysis. All the carbon and water data determined by SIMS are tabulated in Supplementary Table 1. It can be seen from Supplementary Table 1 that the bulk water content in silicate melts is between 0.01 and 1.1 wt%, and the bulk carbon content is between 10 and 240 ppm. Supplementary Fig. 3 shows that the carbon solubility in silicate melt is mainly a function of oxygen fugacity and melt H₂O content. At oxidized conditions ($\log f_{\text{O}_2} > \Delta\text{IW}-1.5$), the carbon solubility in silicate melt decreases with decreasing oxygen fugacity, regardless of melt H₂O content. However, at reduced conditions ($\log f_{\text{O}_2} < \Delta\text{IW}-1.5$), the carbon solubility in silicate melt increases with decreasing oxygen fugacity and with increasing melt H₂O content. The main reason for this observation is that at oxidized conditions, the main carbon species in silicate melt is carbonate, which in silicate melt decreases with decreasing oxygen fugacity; while at reduced conditions, the main carbon species is methane, which is more stable in silicate melt at low oxygen fugacity and high hydrogen fugacity. See the C–H–O volatile species in silicate melt, measured below by Raman and FTIR spectroscopy.

Raman and FTIR spectroscopy were used to determine and quantify the possible C–H–O species in the silicate glasses, following methodologies detailed in recent studies^{5–7,35}. A Renishaw inVia Raman microscope equipped with a 514 nm laser at Rice University was employed^{5,7}, and Raman spectra were collected in the frequency range 200–4,500 cm⁻¹ with 1 cm⁻¹ resolution, using a ×50 objective lens and an output power of 23 mW. The spectrum at each point in this study was accumulated twice with exposure times up to 200–400 s to detect the possible C–H–O species with very low contents.

Typical Raman spectra are shown in Supplementary Fig. 5, which show that at reduced conditions molecular hydrogen (H₂) and methane (CH₄) were present in the silicate melts.

FTIR spectroscopy with a Thermo Nicolet Fourier Transform Infrared Spectrometer was employed following a recent protocol³⁵. Sample glasses were doubly polished to thicknesses of about 200–300 μm. Spectra were recorded with 4 cm⁻¹ resolution, from 650 to 4,000 cm⁻¹, averaging 128 scans. A nitrogen purge was used to eliminate atmospheric gases, with backgrounds collected before each analysis.

Typical FTIR spectra are shown in Supplementary Fig. 5. Supplementary Fig. 5 shows that spectra of silicate glasses synthesized at relatively oxidized conditions contain carbonate doublets at 1,420 and 1,510 cm⁻¹, which are absent for the sample glasses synthesized at relatively reduced conditions. All the spectra had a broad peak at ~3,550 cm⁻¹, indicating the presence of OH⁻ in the glasses. The dissolved OH⁻ content and carbonate content were quantified using the Beer–Lambert law. The extinction coefficient ($\epsilon = 3751 \text{ mol}^{-1} \text{ cm}^{-1}$) for a similar melt composition was used to quantify the carbonate content^{5,7}, and ϵ of 60–90 l mol⁻¹ cm⁻¹ for water at ~3,550 cm⁻¹ were used to quantify the H₂O content⁵. The results showed that the carbon contents in the form of carbonate for the oxidized glasses were ~20–30 ppm, and the OH⁻ (expressed as H₂O) contents in the silicate glasses ranged from ~0.01 to 0.81 wt%, the latter being much lower than the corresponding bulk H₂O contents determined by SIMS, in particular at very reducing conditions (see Supplementary Table 1).

Assuming that the other water is mainly in the form of molecular hydrogen (H₂), the H₂ contents in silicate melt can be calculated. As pointed out in Li *et al.*⁵, the

H₂ content estimated this way provides an upper bound, as clearly a small fraction of the hydrogen not present as OH⁻ or H₂O is present as CH₄, and ‘molecular H₂’ essentially refers to all non-hydroxyl hydrogen in silicate melt. The correlations observed between Raman peak intensities of molecular H₂ and CH₄ in silicate melt and between non-carbonate carbon and molecular H₂ contents in silicate melt indicate that carbon in the silicate melt is mainly dissolved as hydrogenated carbon species methane at reduced conditions (Supplementary Fig. 6).

Estimation of oxygen fugacity. Following the method used in previous studies^{5–7}, the oxygen fugacity (f_{O_2}) prevailing during the experiments was calculated from the coexistence of Fe-rich alloy melt and silicate melt with finite FeO content using the following equilibrium:



from which the f_{O_2} relative to f_{O_2} of the iron-wustite buffer (IW), at any given P – T , can be defined as:

$$\Delta IW = 2 \log(a_{\text{FeO}}/a_{\text{Fe}}) = 2 \log(X_{\text{FeO}}\gamma_{\text{FeO}}/X_{\text{Fe}}\gamma_{\text{Fe}}) \quad (2)$$

a_{FeO} represents the activity of the FeO component in silicate melt; a_{Fe} represents the activity of the Fe component in alloy melt; X_{FeO} and X_{Fe} are the mole fractions of FeO in silicate melt and Fe in alloy melt, respectively; γ_{FeO} and γ_{Fe} are the activity coefficients of FeO in silicate melt and Fe in alloy melt, respectively. Calculations of f_{O_2} using both ideal ($\gamma_{\text{FeO}} = 1$ and $\gamma_{\text{Fe}} = 1$; ideal f_{O_2}) and non-ideal solution models (non-ideal f_{O_2}) were performed. The f_{O_2} calculation using the non-ideal solution model was performed assuming $\gamma_{\text{FeO}} \approx 1.5$ (refs 36,37). Activity coefficients of Fe in Fe-rich melt, γ_{Fe} , were calculated using the ϵ -approach, which takes into account the non-ideal interaction between all the components in the Fe-rich alloy melt^{11,38}. The online ‘Metal Activity Calculator’ (<http://www.earth.ox.ac.uk/~expet/metalact>) provided by the University of Oxford¹¹ was used to calculate the Fe-activity in alloy melt. The calculated ideal f_{O_2} values are in general ~ 0.7 log units lower than the non-ideal f_{O_2} values, and the non-ideal f_{O_2} values of all the runs were between IW-0.7 and IW-5.3 (Supplementary Table 1).

Partition coefficients. $D_{\text{C}}^{\text{alloy/silicate}}$ and $D_{\text{S}}^{\text{alloy/silicate}}$ were calculated based on the measured carbon and sulfur contents in alloy melt and silicate melt. $D_{\text{C}}^{\text{alloy/silicate}}$ varied from 130 to 4,600, while $D_{\text{S}}^{\text{alloy/silicate}}$ varied from 0.4 to 38 (Fig. 1). The $D_{\text{C}}^{\text{alloy/silicate}}/D_{\text{S}}^{\text{alloy/silicate}}$ ratio increases from about 20 to 1,000 as f_{O_2} decreases from IW-0.6 to IW-4.7 (Supplementary Fig. 7).

All the factors controlling carbon dissolution in silicate melt and in Fe-rich alloy melt must control $D_{\text{C}}^{\text{alloy/silicate}}$, including P , T , f_{O_2} , melt water content, compositions of silicate melt and alloy melt. Using all the $D_{\text{C}}^{\text{alloy/silicate}}$ data from this study and those compiled in Fig. 1 of the main text, two empirical

parameterizations were derived. At IW-1.5 $< f_{O_2} < \text{IW}$, $D_{\text{C}}^{\text{alloy/silicate}}$ is mainly a multi-function of P , T , f_{O_2} , compositions of silicate melt and alloy melt:

$$\log D_{\text{C}}^{\text{alloy/silicate}} = 2920/T + 115P/T - 0.66\text{NBO}/T - 0.15\Delta IW - 0.17X_{\text{H}_2\text{O}}^{\text{silicate}} - 2.9X_{\text{Ni}}^{\text{alloy}} + 2.26 \quad (3)$$

whereas at $f_{O_2} < \text{IW-1.5}$, $D_{\text{C}}^{\text{alloy/silicate}}$ is mainly a multi-function of f_{O_2} , melt water content, and composition (Si content) of alloy melt:

$$\log D_{\text{C}}^{\text{alloy/silicate}} = 0.19\Delta IW - 26.9X_{\text{H}_2\text{O}}^{\text{silicate}} - 2.6X_{\text{Si}}^{\text{alloy}} + 4.0 \quad (4)$$

In equations (3) and (4), T is temperature in K, and P is pressure in GPa, X refers to mole fraction, and ΔIW refers to oxygen fugacity relative to the Fe–FeO buffer. Supplementary Fig. 8 shows how well the equations (3) and (4) capture the variability of the experimentally measured $D_{\text{C}}^{\text{alloy/silicate}}$.

Data availability. The authors declare that the data supporting the findings of this study are available within the article and its Supplementary Information files.

References

- Tsuno, K. & Dasgupta, R. Melting phase relation of nominally anhydrous, carbonated pelitic-eclogite at 2.5–3.0 GPa and deep cycling of sedimentary carbon. *Contrib. Mineral. Petrol.* **161**, 743–763 (2011).
- Ding, S., Dasgupta, R. & Tsuno, K. Sulfur concentration of martian basalts at sulfide saturation at high pressures and temperatures—implications for deep sulfur cycle on Mars. *Geochim. Cosmochim. Acta* **131**, 227–246 (2014).
- Dasgupta, R. & Walker, D. Carbon solubility in core melts in a shallow magma ocean environment and distribution of carbon between the Earth’s core and the mantle. *Geochim. Cosmochim. Acta* **72**, 4627–4641 (2008).
- Helo, C., Longpré, M.-A., Shimizu, N., Clague, D. A. & Stix, J. Explosive eruptions at mid-ocean ridges driven by CO₂-rich magmas. *Nat. Geosci.* **4**, 260–263 (2011).
- Duncan, M. S. & Dasgupta, R. CO₂ solubility and speciation in rhyolitic sediment partial melts at 1.5–3.0 GPa—implications for carbon flux in subduction zones. *Geochim. Cosmochim. Acta* **124**, 328–347 (2014).
- O’Neill, H. S. C. & Eggins, S. M. The effect of melt composition on trace element partitioning: an experimental investigation of the activity coefficients of FeO, NiO, CoO, MoO₂ and MoO₃ in silicate melts. *Chem. Geol.* **186**, 151–181 (2002).
- Holzheid, A., Palme, H. & Chakraborty, S. The activities of NiO, CoO and FeO in silicate melts. *Chem. Geol.* **139**, 21–38 (1997).
- Ma, Z. Thermodynamic description for concentrated metallic solutions using interaction parameters. *Metall. Mater. Trans. B* **32**, 87–103 (2001).